Spin-wave interconversion via thermoelectric point-contact control

Takuro Eguchi,[1] Shoki Nezu,[1] Yu Naemura,[2] and Koji Sekiguchi[3,*]

[1]*Graduate School of Engineering Science, Yokohama National University, Tokiwadai 79-5, Yokohama 240-8501, Japan*

[2]*School of Engineering Science, Yokohama National University, Tokiwadai 79-5, Yokohama 240-8501, Japan*

[3]*Faculty of Engineering, Yokohama National University, Tokiwadai 79-5, Yokohama 240-8501, Japan*

(Received 8 March 2022; revised 17 March 2022; accepted 18 July 2022; published 19 August 2022)

The magnonic functionalities of magnonic devices, such as logic gates, majority gates, and multiplexers, critically depend on anisotropic spin-wave dispersions. Further, each magnonic function utilizes the advantages of distinct spin-wave modes. However, thus far, no method of directly combining magnonic functions to construct an integrated magnonic circuit has been proposed. Therefore, this paper presents a method for the interconversion of surface spin-waves and backward volume spin-waves using a thermoelectrically controlled magnetization gradient. The results of time- and frequency-domain spectroscopies, heat transfer analyses, and micromagnetic simulations demonstrate the effectiveness of the proposed method, through which spin-wave interconversion via thermoelectric control may be employed to develop integrated magnonic circuits.

DOI: 10.1103/PhysRevResearch.4.033135

I. INTRODUCTION

Magnonics is a promising field that is expected to lead to the achievement of next-generation information processing (spin-wave computing). Magnons, which are quanta of spin-waves, enable the attainment of low-power-consumption data processing because they are noncharged information carriers. Thus far, many magnonic functionalities have been realized by considering the highly anisotropic spin-wave dispersion relations [1–8]. A previously fabricated magnon transistor employed backward volume magnetostatic spin-waves (BVMSWs) to exploit the nonlinear gating effect [9–12]. In contrast, magnonic majority gates favor the use of forward volume magnetostatic spin-waves (FVMSWs) as an architecture of multiple inputs requiring isotropic propagation with respect to the in-plane magnonic circuit [13,14]. Further, owing to their advantageous features, such as fast propagation and nonreciprocal excitation, magnetostatic surface spin-waves (MSSWs) are often employed in magnonic multiplexers and logic circuits [7,15–19]. Among these modes, FVMSWs require strong magnetic fields to direct magnetization normal to the circuit plane. Such strong magnetic fields can only be produced by traditional electromagnets and affect the overall magnonic device. They cannot be generated by present semiconductor lithography methods for controlling a single nanoscale magnonic circuit, preventing the integration of magnonic functionalities. BVMSWs and MSSWs exhibit substantial potential for the integration of magnonic functionalities because in-plane magnetization can be controlled by a locally generated weak Oersted field or shape magnetic anisotropy. Further, the interconnection between the magnonic functions of BVMSWs and MSSWs is crucial for realizing spin-wave computing.

Pioneering research on the conversion between BVMSWs and MSSWs was conducted using two magnonic waveguide interconnections [8,20–22]. By careful tuning of the direction of the applied magnetic field, an inhomogeneous internal magnetic field was induced in the interconnection areas, and the MSSWs (BVMSWs) propagation were clearly converted into BVMSWs (MSSWs) in a frequency-selective manner. In addition to the structure-induced inhomogeneous magnetization control, another method was developed using a laser-induced magnetization gradient [23–27]. The active (or switchable) heat control promotes the future development of magnonic circuits. However, an inverse conversion method for the active thermal conversion of MSSWs into BVMSWs has not been developed to date. Such a method, which would be a complementary version of the laser-based method, would provide further magnonic functions to fabricate magnonic integrated circuits.

Herein, we report the interconversion of MSSWs and BVMSWs using a thermoelectrically controlled point contact. Compared with the laser-based methods, our method is free from massive laser apparatus containing lasers, mirrors, objective lenses, and piezo elements, which are difficult to implement on integrated chips. Furthermore, the laser-based system provides a single function of heating; however, our method provides the double functions of heating and cooling by employing simple polarity control of the electric current flowing in a single Peltier element. The requirement for the electromagnet to magnetize the magnonic waveguide is the common limitation of integration in both methods, whereas the Peltier element is widely used in ferrimagnetic yttrium iron garnet (YIG)-based generators with a feedback loop to

*sekiguchi-koji-gb@ynu.ac.jp

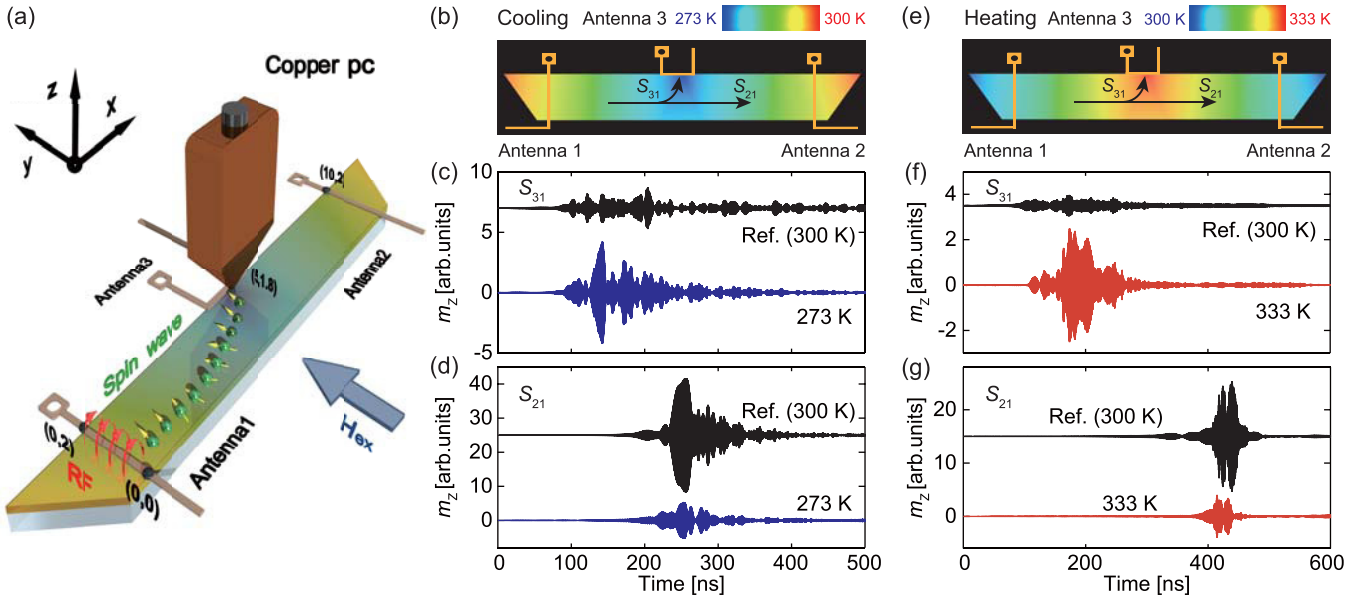

FIG. 1. Simulations of spin-wave properties in temperature gradients. (a) Schematic of our magnonic device architecture. A pure Cu rod was contacted to the YIG waveguide at $(x, y) = (5, 1.8)$ in millimeters. (b) Simulated thermal distribution around the point contact in a cooling process ($T = 273\,\mathrm{K}$), and simulated effect of cooling on transmission signals (c) S_{31} and (d) S_{21}. The carrier frequency of the spin-waves was $\omega/2\pi = 4.683\,\mathrm{GHz}$. (e) Simulated thermal distribution in a heating process ($T = 333\,\mathrm{K}$), and the simulated effect of heating on the transmission signals (f) S_{31} and (g) S_{21}. The carrier frequency of the spin-waves was $\omega/2\pi = 3.468\,\mathrm{GHz}$.

stabilize the temperature-dependent frequency shift [28,29]. The spin-wave interconversion signals are clearly detected via real-time propagating spin-wave spectroscopy and multiport transmission spectroscopy. We demonstrate that thermoelectric control can be employed to control the magnetization gradient in a ferrimagnetic insulator film efficiently. Notably, the method reported in this paper is applicable to miniaturized integrated devices; thus, it can facilitate the development of magnonic integrated circuits.

II. MATERIALS AND METHODS

In our experiment, the spin-wave waveguide was a YIG film with a thickness of $t = 5.1\,\mu\mathrm{m}$, as shown in Fig. 1(a). The YIG film was grown by INNOVENT e.V. Technologieentwicklung Jena, Germany. The length and width of the waveguide were 16.0 and 2.0 mm, respectively. The spin-waves were excited by excitation antenna 1 and detected by antennas 2 and 3. The width of the antenna was 75 μm. Antennas 1 and 2 were located at $x = 0$ and 10 mm, respectively. Antenna 3 was located at ($4 < x < 6\,\mathrm{mm}$, $y = 2\,\mathrm{mm}$).

A Peltier device was connected to the point contact between a pure Cu rod and the YIG waveguide; the contact diameter was 0.5 mm, and the contact center was at (5 mm, 1.8 mm). The temperature of the point contact was monitored by a Pt thermometer. Our scheme is based on the following relations: the magnetization gradient $M_s\,(x, y)$ in the xy plane is induced by thermoelectric cooling and heating $T(x, y)$, and the saturation magnetization M_s is modified as

$$M_s(x, y) = M_{s,300\,\mathrm{K}} - \kappa[T(x, y) - 300\,\mathrm{K}], \qquad (1)$$

where $M_{s,300\,\mathrm{K}}$ is the saturation magnetization of YIG at room temperature (experimentally determined to be $M_{s,300\,\mathrm{K}} = 141\,\mathrm{kA/m}$ using a vibrating sample magnetometer), and κ is a thermomagnetization coupling factor [30]. This calculation was performed by employing the Néel model and verified using the work of Vogel *et al.* [24]. The conversion of MSSWs into BVMSWs was performed by cooling the point contact with a magnetic field in the y direction. In contrast, the conversion of BVMSWs into MSSWs was performed by heating the point contact with a magnetic field in the x direction.

To confirm the effect of the magnetization gradient ∇M on propagating spin-waves, we performed a set of heat transfer analyses and MuMax3 calculations [31]. The thermal distribution of the YIG waveguide under a cooling process is displayed in Fig. 1(b). Note that the temperature near the point contact is approximately $T = 273\,\mathrm{K}$, forming a thermal gradient in the waveguide. Further, the thermal gradient is converted into ∇M according to Eq. (1), with $\kappa = 313\,\mathrm{A/Km}$ [27]. The results of the MuMax3 calculations with ∇M and $H_y = 79.58\,\mathrm{kA/m}$ are shown in Figs. 1(c) and 1(d). The spin-waves were excited by the excitation pulse with a duration of 25 ns, which was also used for subsequent experiments. The carrier frequency of the spin-waves was set to $\omega/2\pi = 4.683\,\mathrm{GHz}$. The z component of the magnetization $\boldsymbol{m}$ on antenna 3, m_z, corresponds to a curved spin-wave signal S_{31}. As shown in Fig. 1(c), there is no spin-wave packet at $T = 300\,\mathrm{K}$. The small signal originates from the excited spin-wave propagating straight near antenna 3, as it covers the edge area and detects the small oscillation of the magnetization at the edge generated by the passing spin-wave. However, a spin-wave packet emerges at $t = 142.4\,\mathrm{ns}$ when the temperature is decreased to $T = 273\,\mathrm{K}$. Further, as shown in Fig. 1(d), m_z on antenna 2, corresponding to S_{21}, exhibits an amplitude that is attenuated by 69% compared with that of the MSSW,

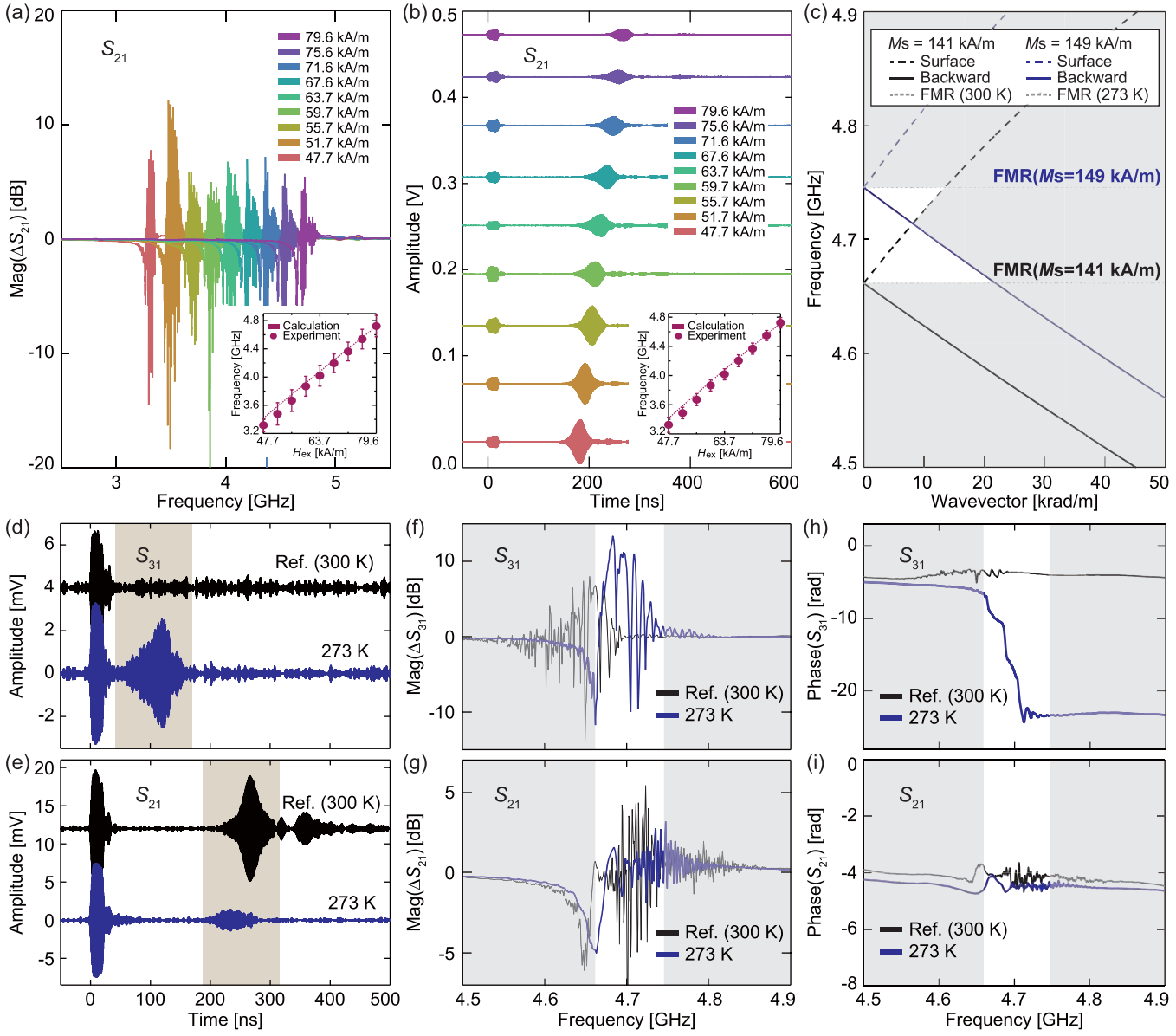

FIG. 2. Conversion from magnetostatic surface spin-waves (MSSWs) into backward volume magnetostatic spin-waves (BVMSWs). (a) Magnetic field dependence of transmission spectra ΔS_{21} of the MSSW. The inset represents the dispersion relation of the MSSW. The error bar represents the width of the resonance spectra. (b) Real-time waveforms of the MSSW in different external magnetic fields. The inset shows the dispersion relation of the MSSW. (c) Schematic of the mixing of spin-wave dispersions via point-contact cooling ($T = 273$ K). Cooling effect on real-time waveforms (d) S_{31} and (e) S_{21}. Cooling effect on the transmission spectra (f) ΔS_{31} and (g) ΔS_{21}. The cooling effect on the phase responses (h) S_{31} and (i) S_{21}. The white area represents the predicted conversion frequency range.

indicating that the MSSW power was efficiently converted into BVMSWs.

For the BVMSW-to-MSSW conversion at $H_x = 51.73$ kA/m, we used a heating process, as shown in Fig. 1(e). The spin-wave carrier frequency was set to $\omega/2\pi = 3.468$ GHz. As shown in Fig. 1(f), there is no spin-wave packet in S_{31} at $T = 300$ K; however, a spin-wave packet emerges at $t = 173.7$ ns upon increasing the temperature to $T = 333$ K. Figure 1(g) displays the 67% attenuated amplitude of straight BVMSW signal S_{21}, showing a conversion effect like that in the cooling process.

III. RESULTS AND DISCUSSION

Figure 2(a) shows the magnetic field (H_y) dependence of typical transmission spectra ΔS_{21} in the MSSW configuration. As the spectra ΔS_{21} represent the property of incident spin-waves, the resonance frequency (f) was analyzed using the formula [32]:

$$f_{\mathrm{MSSW}} = \frac{\mu_0 \gamma}{2\pi} \sqrt{\left(H_y + \frac{M_s}{2}\right)^2 - \left(\frac{M_s}{2}\right)^2 \exp\left(-2kd\right)}, \quad (2)$$

where μ_0 is the permeability in vacuum, $\gamma = 2.21 \times 10^5$ Hz/(A/m), $M_s = 141$ kA/m, $k = 8474$ rad/m, and

$d = 5.1$ μm. As shown in the inset, the f-H curve agrees with the MSSW dispersion. As shown in Fig. 2(b), the real-time waveforms of the incident spin-waves also prove the propagation of MSSWs, as the group velocity decreases as the magnetic field increases. The dispersion relation of MSSWs is also reproduced by the fast Fourier transform (FFT) analysis (see inset).

Figure 2(c) presents a diagram of MSSW-BVMSW conversion at $H_y = 79.58$ kA/m. Cooling the point contact to $T = 273$ K introduces a magnetization gradient ∇M in the YIG film, and the frequency $\omega[M_s(\mathrm{T})]$ for BVMSWs forms a band between the BVMSW dispersion curves with maximum $M_s = 149$ kA/m (solid blue line) and minimum $M_s = 141$ kA/m (solid black line). The frequency $\omega[M_s(\mathrm{T})]$ for MSSWs forms a band between the MSSW dispersion curves with maximum $M_s = 149$ kA/m (broken blue line) and minimum $M_s = 141$ kA/m (broken black line). Because ∇M also introduces a change in magnetization direction, the spin-wave dispersions mix in the white area shown in Fig. 2(c). As discussed in detail by Vogel *et al.* [24], the conversion frequency range is regulated by low-energy resonance, particularly the ferromagnetic resonance frequency (dotted lines). For the time-resolved measurement of spin-wave conversion [33], we transmitted pulse-modulated radiofrequency (RF) signals with $\omega/2\pi = 4.683$ GHz, power $P_{\mathrm{rf}} = 5$ dBm, and duration $\Delta t = 25$ ns to antenna 1.

Figure 2(d) shows the real-time spin-wave waveforms detected by antenna 3 (S_{31}). At room temperature ($T = 300$ K), there was no spin-wave packet, as shown by the solid black line. When the point contact cooled to $T = 273$ K, a clear spin-wave packet with a 2.559 mV amplitude emerged at $t = 119.5$ ns, as shown by the solid blue line. The amplitude and arriving time of the packet were defined by the maximum signal position. The group velocity of the spin-wave packets was deduced as follows: $v_g(T = 273\ \mathrm{K}) = l_{13}/119.5\ \mathrm{ns} = 42$ km/s, where $l_{13} = 5$ mm is assumed to be the median value of the propagation distance between antennas 1 and 3. This value agrees with the analytically calculated $v_g(T = 273\ \mathrm{K}) = 41$ km/s for MSSWs. Note that the signal at $0 < t < 25$ ns originates from direct coupling between the excitation and detection antennas, which is caused by the electromagnetic waves at the speed of light [7].

Figure 2(e) shows the real-time waveforms detected by antenna 2 (S_{21}). We can observe a spin-wave packet at 265.7 ns and an electromagnetic excitation signal at $0 < t < 25$ ns. The amplitude of the spin-wave packet decreases from 6.947 to 1.458 mV, exhibiting 81% attenuation. The group velocity at 300 K was deduced to be 38 km/s, which agrees with the calculated $v_g(T = 300\ \mathrm{K}) = 38$ km/s for MSSWs. This finding demonstrates that S_{21} originated from the initially input spin-waves.

To check the validity of our experiment, the transmission spectra were measured using a vector network analyzer. Figure 2(f) depicts transmission signal ΔS_{31} measured with $P_{\mathrm{rf}} = 5$ dBm. Under point-contact cooling to $T = 273$ K, the ΔS_{31} ($T = 273$ K) spectrum is exactly located in the conversion frequency range $4.662 < \omega/2\pi < 4.746$ GHz, whereas ΔS_{31} ($T = 300$ K) is out of this range. By choosing an appropriate carrier frequency, e.g., $\omega/2\pi = 4.683$ GHz, the MSSWs can be efficiently converted into BVMSWs. Figure 2(g) shows the transmission (MSSW) signal ΔS_{21}. Compared with the magnitude of $\Delta S_{21}(T = 300\ \mathrm{K})$ in the conversion frequency range ($4.662 < \omega/2\pi < 4.746$ GHz), the magnitude of $\Delta S_{21}(T = 273\ \mathrm{K})$ is clearly diminished, indicating that the MSSWs decreased in magnitude owing to the BVMSW conversion. Figure 2(h) shows the phase signals of S_{31}. The phase of S_{31} at 300 K originates from an excited MSSW and shows a small but positive increase of the phase $d\varphi/df > 0$, whereas that of ΔS_{31} at 273 K shows a large phase decrease $d\varphi/df < 0$, illustrating the propagation of the BVMSW. As shown in Fig. 2(i), S_{21} simply shows the propagations of excited MSSWs and represents small but positive phase shifts. As reported by Sadovnikov *et al.* [21], these phase responses are characteristic of spin-wave modes.

Next, we present the results of the complementary experiment. Figure 3(a) shows the magnetic field (H_x) dependence of typical transmission spectra ΔS_{21} in the BVMSW configuration. The resonance frequency (f) was analyzed using the formula [32]:

$$f_{\mathrm{BVMSW}} = \frac{\mu_0 \gamma}{2\pi} \sqrt{H_x \left\{ H_x + M_S \left[\frac{1 - \exp(-kd)}{kd} \right] \right\}}, \quad (3)$$

where μ_0 is the permeability in vacuum, $\gamma = 2.21 \times 10^5$ Hz/(A/m), $M_s = 141$ kA/m, $k = 11070$ rad/m and $d = 5.1$ μm. As shown in the inset, the f-H curve agrees with the BVMSW dispersion. As shown in Fig. 3(b), the real-time waveforms of the incident spin-waves also prove the propagation of the BVMSW because the group velocity increases as the magnetic field increases. The dispersion relation of the BVMSW is also reproduced by the FFT analysis (see inset).

Figure 3(c) presents a diagram of the conversion of a BVMSW into a MSSW at $H_x = 51.73$ kA/m. The point-contact heating ($T = 333$ K) introduces the magnetization gradient ∇M and mixes the spin-wave dispersions. We transmitted pulse-modulated RF signals with $\omega/2\pi = 3.468$ GHz, power $P_{\mathrm{rf}} = 5$ dBm, and duration $\Delta t = 25$ ns.

The real-time spin-wave waveforms are presented in Figs. 3(d) and 3(e). As shown in Fig. 3(d), when the point contact was heated to $T = 333$ K, a spin-wave packet could be observed at $t = 193.6$ ns. The deduced group velocity is $v_g = 26$ km/s, which is slightly larger than the analytical group velocity $v_g = 20$ km/s for BVMSWs, suggesting that the converted MSSW is detected at closer positions, $l_{13} < 5$ mm. Under point-contact heating, the amplitude of the wave packet at antenna 3 is clearly enhanced to 1.679 mV, evidently yielding an on/off ratio. At antenna 2, as shown in Fig. 3(e), the attenuation of the BVMSW is clearly detected. The amplitude decreases from 1.725 to 0.393 mV, corresponding to 77% attenuation. The group velocity is 20 km/s, which is in accordance with the analytically determined value $v_g = 20$ km/s for the initial BVMSW.

Figure 3(f) shows the transmission spectrum for ΔS_{31}. Under point-contact heating, as shown by the solid red line, the magnitude of $\Delta S_{31}(T = 333\ \mathrm{K})$ is clearly enhanced in the conversion frequency range $3.411 < \omega/2\pi < 3.513$ GHz. In contrast, $\Delta S_{31}(T = 300\ \mathrm{K})$ is out of this range, and the carrier frequency $\omega/2\pi = 3.468$ GHz can be converted with a high on/off ratio. Figure 3(g) presents the transmission spectrum for ΔS_{21} (BVMSWs). Compared with the

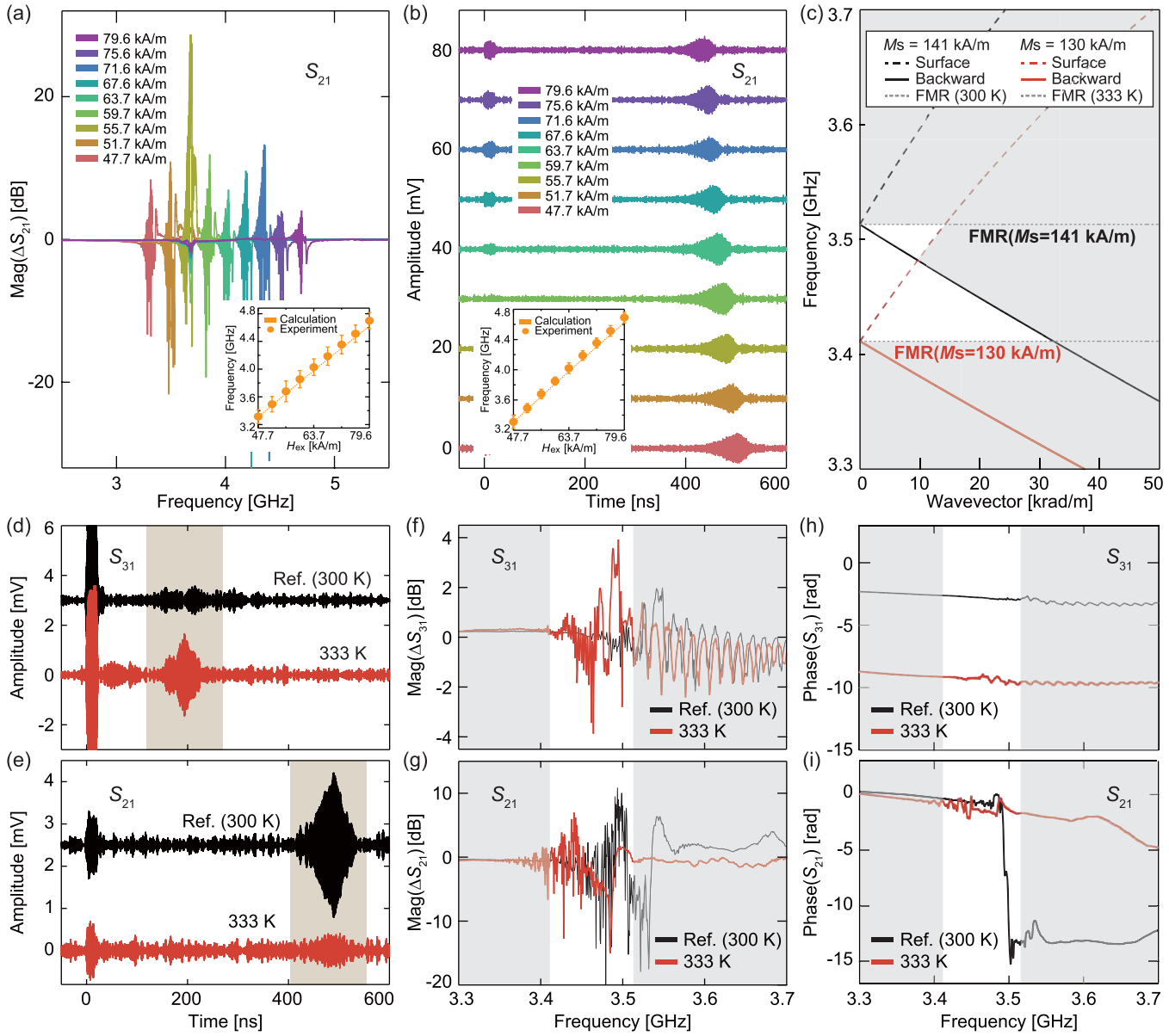

FIG. 3. Conversion from backward volume magnetostatic spin-waves (BVMSWs) to magnetostatic surface spin-waves (MSSWs). (a) Magnetic field dependence of transmission spectra ΔS_{21} of the BVMSW. The inset represents the dispersion relation of the BVMSW. (b) Real-time waveforms of the BVMSW in different external magnetic fields. The inset shows the dispersion relation of the BVMSW. (c) Schematic of spin-wave dispersion mixing via point-contact heating ($T = 333$ K). Heating effect on real-time waveforms (d) S_{31} and (e) S_{21}. Heating effect on transmission spectra (f) ΔS_{31} and (g) ΔS_{21}. Heating effect on the phase responses (h) S_{31} and (i) S_{21}. The white area represents the predicted conversion frequency range.

magnitude of $\Delta S_{21}(T = 300\,\mathrm{K})$ in the conversion frequency range $3.411 < \omega/2\pi < 3.513$ GHz, the resonance magnitude of $\Delta S_{21}(T = 333\,\mathrm{K})$ is diminished. This characteristic indicates that BVMSW lost its magnitude owing to MSSW conversion. Figure 3(h) shows the phase signals of S_{31}. The phase of S_{31} at 333 K shows a small but positive phase increase, $d\varphi/df > 0$, proving the propagation of the converted MSSW. As shown in Fig. 3(i), the phase of S_{21} at 300 K had a large phase decrease, $d\varphi/df < 0$, proving the passing of the excited BVMSW.

The relationship between the temperature gradient and spin-wave modes was experimentally investigated; the results are summarized in the Supplemental Material [33]. No spin-wave signals were converted from the BVMSW to the MSSW configuration in the cooling gradient and from the MSSW to the BVMSW configuration in the heating gradient. These experiments also verify that the results presented in this paper originate from spin-wave interconversion. Another effect on the interconversion, that is, lateral confinement, is also presented in the Supplemental Material [33], and it was revealed to cause no crucial differences.

Finally, the point-contact-temperature T dependence of spin-wave interconversion was analyzed, as presented in Fig. 4. To deduce the conversion signal-to-noise ratio (SNR), the power-spectral density $p(\omega)$ was calculated using the time-domain waveform of the spin-wave packets, as each packet

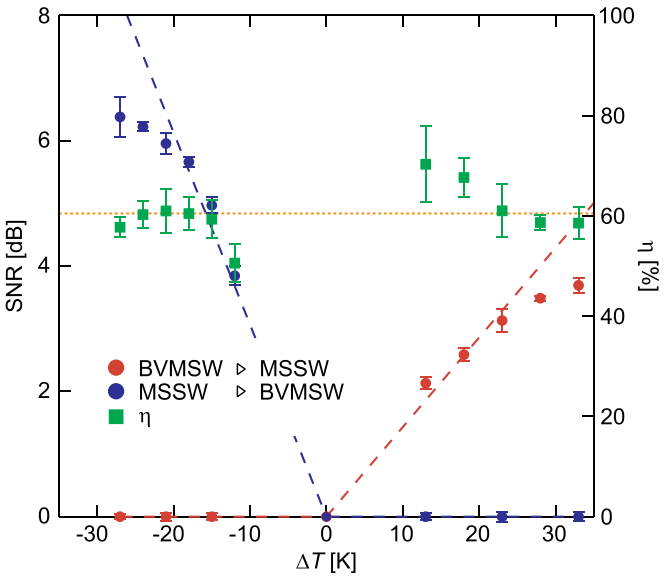

FIG. 4. Temperature dependence of signal-to-noise ratio and conversion ratio. The broken lines show the linear fits. The region in which the temperature is negative corresponds to the conversion of magnetostatic surface spin-waves (MSSWs) into backward volume magnetostatic spin-waves (BVMSWs), whereas the region where the temperature is positive corresponds to the conversion of BVMSWs to MSSWs. Each point represents the average of 10 independent measurements. The averaged conversion ratio of 60.5% is depicted by a dotted line.

exhibits the frequency dispersion near the carrier frequency:

$$\mathrm{SNR(dB)} = 10\log_{10}\left(\frac{P_{S_{31},T}}{P_{S_{31},300\,\mathrm{K}}}\right) = 10\log_{10}\left[\frac{\int p_{S_{31},T}(\omega)d\omega}{\int p_{S_{31},300\,\mathrm{K}}(\omega)d\omega}\right], \quad (4)$$

where $P_{S_{31},T}$ and $P_{S_{31},300\,\mathrm{K}}$ represent the total power of packet S_{31} at temperatures T and 300 K, respectively, and $p_{S_{31},T}(\omega)$ and $p_{S_{31},300\,\mathrm{K}}(\omega)$ are the power-spectral densities at temperatures T and 300 K, respectively. Further, the conversion ratio η was defined as follows:

$$\left(P_{S_{31},T} - P_{S_{31},300\,\mathrm{K}}\right) = -\eta\left(P_{S_{21},T} - P_{S_{21},300\,\mathrm{K}}\right). \quad (5)$$

To evaluate the SNR and conversion ratio, two important points were considered. The S_{31} and S_{21} signals were attenuated by the magnetic damping during approximately 5.0 and 1.0 mm propagation, corresponding to the distances from the point contact to antennas 3 and 2 (half of length and width). The magnetic damping itself was modulated by cooling and heating. By measuring the propagation distance and temperature dependences of the spin-wave amplitude, as shown in the Supplemental Material [33], we compensated for these effects.

Figure 4 shows that the SNR exhibits a linear dependence on ΔT ($= T - 300\,\mathrm{K}$). The gains are 6.38 dB at $\Delta T = -27\,\mathrm{K}$ and 3.69 dB at $\Delta T = 33\,\mathrm{K}$. Compared with the cooling process, the heating process showed smaller magnitudes of gain, possibly owing to the leakage of the BVMSW signal in S_{31} at 300 K. The reason for the small leakage of the BVMSW signal in our geometry was not resolved experimentally. However, if this leakage signal vanishes, the SNR would have the same magnitude in both the cooling and heating processes. The SNRs at $\Delta T = -27\,\mathrm{K}$ deviate from the linear dependence and show smaller magnitudes. This is because the temperature gradient in the YIG waveguide was saturated because of the finite thermal conductivity of YIG. This feature was also observed upon heating to $\Delta T = 33\,\mathrm{K}$, where a decrease in the temperature gradient resulted in a lower magnitude of SNR. On the contrary, the conversion ratio η exhibits an approximately constant value of 60.5% in both the cooling and heating processes. The exact value of the conversion ratio could be improved if we can develop the geometry of antenna 3 to detect the entire signal of vending spin-waves. However, this proves that the physics of conversion due to the thermal gradient ∇T, i.e., the magnetization gradient ∇M, was unchanged because the conversion represents the angular momentum transfer from one mode to another, or the magnons simply changed their propagating direction. The linear dependence of the conversion SNR on ∇T demonstrates that spin-wave interconversion via thermoelectric control is a robust method.

IV. CONCLUSIONS

The spin-wave interconversions via thermoelectric point-contact control were demonstrated using a time-domain spin-wave experiment. The conversion SNR and conversion ratio were directly evaluated based on the waveforms of the spin-wave packets. The thermoelectric point contact clearly controlled the transmission of the spin-wave packet. The frequency-domain experiment detected the mixing of the spin-wave bands and transmissions. The modes of the converted spin-waves were confirmed by the phase response of the transmission signals. The agreements with micromagnetic and analytical calculations supported the interconversion mechanism. In this paper, the point-contact temperature was controlled using a conventional electric Peltier element; however, with further improvements of point contact, the proposed technique will be able to serve as a standard method for combining magnonic circuits.

ACKNOWLEDGMENTS

This paper was supported by the Grants-in-Aid for Scientific Research (No. 19H00861 and No. 18H05346) from the Japan Society for the Promotion of Science. K.S. acknowledges the support by Grants-in-Aid for Scientific Research (No. 20H05652).

T.E. and K.S. planned the experiment. T.E., Y.N., and K.S. designed and prepared the samples and performed the time- and frequency-domain spin-wave spectroscopies. T.E. performed the numerical calculations to predict the thermal effect on the spin-wave propagation. T.E., S.N., and K.S. wrote the paper. All authors discussed the results.

APPENDIX A: TIME- AND FREQUENCY-DOMAIN PROPAGATING SPIN-WAVE SPECTROSCOPIES

For the time-resolved measurement of spin-wave conversion, we transmitted pulse-modulated RF signals with $\omega/2\pi = 3.468$ and 4.683 GHz and duration $\Delta t = 25\,\mathrm{ns}$ to

antenna 1. The propagating spin-wave signals were detected as induced voltages by a 6 GHz real-time oscilloscope. Multiport transmission spectroscopy was performed with a vector network analyzer (Agilent Technology, N5230A). To enhance the signal clarity, we used a background subtraction procedure, i.e., the background-subtracted transmission signals $\Delta S_{31} = S_{31}(H) - S_{31}(H = 0)$ and $\Delta S_{21} = S_{21}(H) - S_{21}(H = 0)$ were employed to detect the MSSWs and converted BVMSWs, respectively.

APPENDIX B: HEAT TRANSFER ANALYSIS

The thermal distribution in our sample was calculated using Fusion360. The thermal conductivities for the YIG, GGG substrate, and Cu point contact were $\lambda_{\mathrm{YIG}} = 7.4\,\mathrm{W/mK}$, $\lambda_{\mathrm{GGG}} = 7.05\,\mathrm{W/mK}$, and $\lambda_{\mathrm{Cu}} = 403\,\mathrm{W/mK}$, respectively.

APPENDIX C: MICROMAGNETIC SIMULATION

Micromagnetic simulations were performed by numerically solving the Landau-Lifshitz-Gilbert equation, $\partial\mathbf{m}/\partial t = -\gamma_g\mu_0\mathbf{m} \times \mathbf{H}_{\mathrm{eff}} + \alpha_G\mathbf{m} \times \partial\mathbf{m}/\partial t$, where $\mathbf{m}$ is the unit vector along the magnetization, $\mathbf{H}_{\mathrm{eff}}$ is the effective magnetic field including the exchange, magnetostatic, and external fields, and α_G is the Gilbert damping. The following parameters were used: dimensions of the YIG film $= 12\,\mathrm{mm} \times 2.1\,\mathrm{mm} \times 5.1\,\mu\mathrm{m}$; number of cells $= 1024 \times 512 \times 1$; $\alpha_G = 0.0001$; exchange stiffness constant $A_{\mathrm{ex}} = 3.7 \times 10^{-12}\,\mathrm{J/m}$; and saturation magnetization $M_s = 1.41 \times 10^5\,\mathrm{A/m}$. A different cell size with a different number of cells $= 1024 \times 512 \times 5$ had a longer calculation time but gave the same spin-wave packet reduction ratio, except for the detailed shape of the packet.

[1] A. G. Gurevich and G. A. Melkov, *Magnetization Oscillations and Waves* (CRC Press, London, 1996).

[2] A. V. Chumak, V. I. Vasyuchka, A. A. Serga, and B. Hillebrands, Magnon spintronics, Nat. Phys. **11**, 453 (2015).

[3] V. V. Kruglyak, S. O. Demokritov, and D. Grundler, Magnonics, J. Phys. D: Appl. Phys. **43**, 264001 (2010).

[4] A. Khitun, M. Bao, and K. L. Wang, Magnonic logic circuits, J. Phys. D: Appl. Phys. **43**, 264005 (2010).

[5] B. Lenk, H. Ulrichs, F. Garbs, and M. Munzenberg, The building blocks of magnonics, Phys. Rep. **507**, 107136 (2011).

[6] M. Krawczyk and D. Grundler, Review and prospects of magnonic crystals and devices with reprogrammable band structure, J. Phys.: Condens. Matter **26**, 123202 (2014).

[7] K. Sekiguchi, K. Yamada, S. M. Seo, K. J. Lee, D. Chiba, K. Kobayashi, and T. Ono, Nonreciprocal emission of spin-wave packet in FeNi film, Appl. Phys. Lett. **97**, 022508 (2010).

[8] A. V. Sadovnikov, A. A. Grachev, V. A. Gubanov, S. A. Odintsov, A. A. Martyshkin, S. E. Sheshukova, Yu. P. Sharaevskii, and S. A. Nikitov, Spin-wave intermodal coupling in the interconnection of magnonic units, Appl. Phys. Lett. **112**, 142402 (2018).

[9] N. Sato, S. W. Lee, K. J. Lee, and K. Sekiguchi, Current-induced modulation of backward spin-waves in metallic microstructures, J. Phys. D: Appl. Phys. **50**, 094004 (2017).

[10] A. V. Chumak, T. Neumann, A. A. Serga, B. Hillebrands, and M. P. Kostylev, A current-controlled, dynamic magnonic crystal, J. Phys. D: Appl. Phys. **42**, 205005 (2009).

[11] A. V. Chumak, A. A. Serga, and B. Hillebrands, Magnon transistor for all-magnon data processing, Nat. Commun. **5**, 4700 (2014).

[12] M. Iwaba and K. Sekiguchi, Spin-wave switching using dynamic magnonic crystal, Appl. Phys. Exp. **14**, 073002 (2021).

[13] N. Kanazawa, T. Goto, K. Sekiguchi, A. B. Granovsky, C. A. Ross, H. Takagi, Y. Nakamura, H. Uchida, and M. Inoue, The role of Snell's law for a magnonic majority gate, Sci. Rep. **7**, 7898 (2017).

[14] K. Sekiguchi, D. Chiba, and T. Tachizaki, Time-domain propagating spin-wave spectroscopy for forward spin waves in a ferromagnetic metal, Jpn. J. Appl. Phys. **57**, 0902B4 (2018).

[15] K. Vogt, F. Y. Fradin, J. E. Pearson, T. Sebastian, S. D. Bader, B. Hillebrands, A. Hoffmann, and H. Schultheiss, Realization of a spin-wave multiplexer, Nat. Commun. **5**, 3727 (2014).

[16] C. Liu, J. Chen, T. Liu, F. Heimbach, H. Yu, Y. Xiao, J. Hu, M. Liu, H. Chang, T. Stueckler *et al.*, Long-distance propagation of short-wavelength spin waves, Nat. Commun. **9**, 738 (2018).

[17] C. L. Ordonez-Romero, Z. Lazcano-Ortiz, A. Drozdovskii, B. Kalinikos, M. Aguilar-Huerta, J. L. Domínguez-Juárez, G. Lopez-Maldonado, N. Qureshi, O. Kolokoltsev, and G. Monsivais, Mapping of spin wave propagation in a one-dimensional magnonic crystal, J. Appl. Phys. **120**, 043901 (2016).

[18] N. Sato and K. Sekiguchi, Electrical demonstration of spin-wave logic operation, Appl. Phys. Express. **6**, 063001 (2013).

[19] K. Sekiguchi, S.-W. Lee, H. Sukegawa, N. Sato, S.-H. Oh, R. D. McMichael, and K.-J. Lee, Spin-wave propagation in cubic anisotropic materials, NPG Asia Materials **9**, e392 (2017).

[20] A. V. Sadovnikov, C. S. Davies, S. V. Grishin, V. V. Kruglyak, D. V. Romanenko, Yu. P. Sharaevskii, and S. A. Nikitov, Magnonic beam splitter: the building block of parallel magnonic circuitry, Appl. Phys. Lett. **106**, 192406 (2015).

[21] A. V. Sadovnikov, C. S. Davies, V. V. Kruglyak, D. V. Romanenko, S. V. Grishin, E. N. Beginin, Y. P. Sharaevskii, and S. A. Nikitov, Spin wave propagation in a uniformly biased curved magnonic waveguide, Phys. Rev. B **96**, 060401(R) (2017).

[22] A. A. Martyshkin, E. N. Beginin, A. I. Stognij, S. A. Nikitov, and A. V. Sadovnikov, 3D magnonic network: vertical spin-wave transport in the magnonic waveguides with broken translation symmetry, IEEE Magn. Lett. **10**, 5511105 (2019).

[23] O. Dzyapko, I. V. Borisenko, V. E. Demidov, W. Pernice, and S. O. Demokritov, Reconfigurable heat-induced spin wave lenses, Appl. Phys. Lett. **109**, 232407 (2016).

[24] M. Vogel, A. V. Chumak, E. H. Waller, T. Langner, V. I. Vasyuchka, B. Hillebrands, and G. von Freymann, Optically reconfigurable magnetic materials, Nat. Phys. **11**, 487 (2015).

[25] B. Obry, V. I. Vasyuchka, A. V. Chumak, A. A. Serga, and B. Hillebrands, Spin-wave propagation and transformation in a thermal gradient, Appl. Phys. Lett. **101**, 192406 (2012).

[26] E. H. Waller and G. V. Freymann, Multi foci with diffraction limited resolution, Opt. Express **21**, 21708 (2013).

[27] M. Vogel, R. Aßmann, P. Pirro, A. V. Chumak, B. Hillebrands, and G. von Freymann, Control of spin-wave propagation using magnetisation gradients, Sci. Rep. **8**, 11099 (2018).

[28] D. W. Peterman, M. Ye, and P. E. Wigen, Controlling high frequency chaos in circular YIG films, J. Appl. Phys. **76**, 6886 (1994).

[29] W. Ishak, E. Reese, R. Baer, and M. Fowler, Tunable magnetostatic wave oscillators using pure and doped YIG films, IEEE Trans. Magn. **20**, 5 (1984).

[30] E. E. Anderson, Molecular field model and the magnetization of YIG, Phys. Rev. **134**, A1581 (1964).

[31] A. Vansteenkiste, J. Leliaert, M. Dvornik, M. Helsen, F. Garcia-Sanchez, and B. Van Waeyenberge, The design and verification of MuMax3, AIP Adv. **4**, 107133 (2014).

[32] D. D. Stancil and A. Prabhakar, *Spin Waves: Theory and Applications* (Springer, New York, 2009).

[33] See Supplemental Material at http://link.aps.org/supplemental/10.1103/PhysRevResearch.4.033135 for additional experimental results including temperature dependence of resonant frequency, spin-wave transmission experiment in complementary conditions, and temperature dependence of magnetic damping in YIG film.